Journal of Materials Chemistry A

RSC Publishing

PAPER

View Article Online
View Journal

Published on 20 June 2013. Downloaded by Universitat Politècnica de València on 29/07/2013 11:46:36.

Cite this: DOI: 10.1039/c3ta11610g

Bulk transport and oxygen surface exchange of the mixed ionic–electronic conductor $Ce_{1-x}Tb_xO_{2-\delta}$ ($x = 0.1, 0.2, 0.5$)†

María Balaguer,[a] Chung-Yul Yoo,[b] Henny J. M. Bouwmeester[b] and Jose M. Serra*[a]

Received 23rd April 2013
Accepted 16th June 2013

DOI: 10.1039/c3ta11610g

www.rsc.org/MaterialsA

Bulk ionic and electronic transport properties and the rate of oxygen surface exchange of Tb-doped ceria have been evaluated as a function of Tb concentration, aiming to assess the potential use of the materials as high-temperature oxygen-transport membranes and oxygen reduction catalysts. The materials were synthesized by the co-precipitation method. Cobalt oxide (2 mol%) was added in order to improve sinterability and conductivity. The materials were studied by means of X-ray diffraction (XRD), temperature-programmed desorption (TPD), thermogravimetry (TG), DC-conductivity and UV-vis spectrophotometry. The results indicate that the extent of mixed ionic–electronic conductivity is a function of temperature and can be tuned by modifying the Tb- (and Co-doping) concentration. Low Tb-content materials ($x = 0.1$ and 0.2) are predominant ionic conductors, but the materials with 50 mol% Tb show both p-type electronic and ionic conductivity. The enhanced electronic conduction in $Ce_{0.5}Tb_{0.5}O_{2-\delta}$ is associated with narrowing of the band gap upon doping ceria with Tb. In addition, the surface chemistry of the samples was investigated by means of X-ray photoelectron spectroscopy (XPS) and pulse isotopic exchange (PIE). The surface exchange rate is found to increase on increasing the level of Tb doping. The highest surface exchange rates in this study are found for materials doped with 50 mol% Tb.

Introduction

Oxygen separation technologies based on ion transport membranes enable thermal integration and energy savings in oxyfuel power plants and other energy-intensive processes.[1,2] Membranes based on mixed ionic electronic conductor (MIEC) materials enable *in situ* separation of oxygen.[3,4] Commonly used MIEC membrane materials include thermally stable perovskites *e.g.* $Ba_{1-x}Sr_xCo_{0.8}Fe_{0.2}O_{3-\delta}$ (BSCF) and $La_{1-x}Sr_xCo_{0.8}Fe_{0.2}O_{3-\delta}$ (LSCF).[5] High oxygen fluxes up to 9.5 ml cm^{-2} min^{-1} at 1223 K can be achieved using BSCF hollow fibres and asymmetric membranes.[6–8] Using LSCF hollow fibres, a flux of 3.2 ml cm^{-2} min^{-1} (LSCF) has been reported at 1173 K.[9] In both cases argon was used as sweep gas. However, the listed materials are limited by poor chemical stability under the large oxygen concentration gradient encountered during membrane operation, with one side of the membrane exposed to pressurized air and the other side to a reducing or CO_2-containing atmosphere.[10–12] Even at a concentration of 300 ppm, the presence of CO_2 is a major issue for, *e.g.*, BSCF due to the carbonation reaction associated with the presence of earth alkali metals in the perovskite structure.[13]

Alternatively, lanthanide-substituted ceria materials combine rather high oxygen-ion conductivities, redox catalytic properties and chemical compatibility with water and CO_2 at high temperatures. In addition, they show n-type electronic conductivity due to partial reduction of ceria ions, from the tetravalent to the trivalent state, at high temperatures under reducing conditions ($pO_2 < 10^{-10}$ atm). Electron transport is facilitated by hopping between cerium sites *via* a small polaron process. Doping ceria with multivalent cations allows extension of the mixed ionic–electronic conduction to higher oxygen partial pressures (10^{-5} to 10^{-1} atm), which enables its application as an oxygen permeable membrane.[14] Praseodymium and terbium are suitable dopants. Their doping into ceria has been previously studied by Fagg *et al.*,[15] Chatzichristodoulou *et al.*[16] and Balaguer *et al.*[17] Ceria-based membranes offer competitive oxygen permeation fluxes at

[a]Instituto de Tecnología Química (Universidad Politécnica de Valencia – Consejo Superior de Investigaciones Científicas), av. Los Naranjos s/n, E-46022 Valencia, Spain. E-mail: jmserra@itq.upv.es; Fax: +34 96 3879444; Tel: +34 96 3879448

[b]Inorganic Membrane, Faculty of Science and Technology, MESA+ institute for nanotechnology, University of Twente, 7500 AE, The Netherlands

† Electronic supplementary information (ESI) available: Fig. S1 shows the XRD patterns of the materials sintered at 1723 K. Any impurity or secondary phase was observed up to the limit of the apparatus. Fig. S2 shows the scanning microscope images of CTx and CTCox taken by a backscatter electron detector, and the grain boundary details of the CTxCo samples. Fig. S3 shows the Arrhenius plot of the total conductivity in air for the Tb doped series. Fig. S4 depicts the comparison between Ce 3d XPS spectra of CT20 and CT20Co. Fig. S5 shows the O 1s XPS spectra of CT20 and CT20Co, composed of two components. Fig. S6 represents the oxygen surface exchange rate as a function of the oxygen non-stoichiometry at 973 K for the 6 samples analysed in this work. Finally, Fig. S7 illustrates the dependence of the rates of dissociative adsorption ($\Re_a$) and oxygen incorporation ($\Re_i$) on the inverse temperature for the terbium doped series studied. See DOI: 10.1039/c3ta11610g

Published on 20 June 2013. Downloaded by Universitat Politècnica de València on 29/07/2013 11:46:36.

temperatures below 1123 K when compared with perovskite-based membranes.[18,19]

Basic requirements for oxygen permeation are fast kinetics for bulk oxygen transport, *e.g.*, *via* oxygen defect sites, and electron and/or electron–hole transport, as well as fast surface oxygen exchange kinetics, involving dissociation of molecular O_2, its reduction to oxygen adatoms, and successive incorporation into the oxide lattice as O^{2-} anions. Bulk oxygen transport and oxygen surface exchange are characterized by two kinetic parameters, *i.e.*, diffusion coefficient D ($cm^2\ s^{-1}$) and surface exchange coefficient k ($cm\ s^{-1}$). Different techniques have been developed in order to determine these parameters. Commonly used techniques include isotopic exchange depth profiling using, *e.g.*, secondary ion mass spectrometry (SIMS) and electrical conductivity relaxation (ECR).[20–22,49] Pulse isotopic exchange (PIE)[23] and isothermal oxygen isotope equilibration[24] techniques allow working in a surface exchange-dominated regime provided that powders are employed with a particle size smaller than the so-called characteristic thickness ($L_c = D/k$).[25]

In this work, different compositions of $Ce_{1-x}Tb_xO_{2-\delta}$ (x = 0.1, 0.2, 0.5), either undoped or cobalt-doped, have been prepared and characterized to assess its applicability as an oxygen separation membrane. Several bulk-related properties were investigated to gain insight into the transport properties of terbium-doped ceria. These were investigated by means of X-ray diffraction (XRD), temperature-programmed desorption (TPD), thermogravimetry (TG), DC-conductivity and UV-vis spectrophotometry. The surface chemistry of the samples was studied by X-ray photoelectron spectroscopy (XPS). Pulse isotopic exchange (PIE) experiments were conducted to measure the rate of oxygen surface exchange.

Experimental methods

Terbium-doped ceria compounds were prepared by the co-precipitation method. A clear solution of commercial lanthanide nitrates in the appropriate cation ratio was prepared with distilled water at 323 K. A $(NH_4)_2CO_3$ solution was dropped into the previous solution to achieve precipitation and the final NO_3^-/CO_3^{2-} molar ratio was 0.75. The resulting precursor powders were dried at 373 K after filtration and rinsing with water. The cobalt addition (when required) was done over the dried precursor powder by incipient wetness impregnation. $Co(NO_3)_2 \cdot 6H_2O$ was dissolved in distilled water, and then the powder was impregnated until incipient wetness using this solution. Finally, each powder was calcined for 5 h in air at 1073 K to decompose the residual nitrates and carbonates, and to favour the formation of the fluorite phase. In this study, $Ce_{1-x}Tb_xO_{2-\delta}$ samples are referred to as CTx and CTxCo, for Co-free and Co-containing samples, respectively.

To identify the crystalline phase and the lattice parameters of the samples, the powders were characterized by X-ray diffraction (XRD). The measurements were carried out on a PANalytical CubiX fast diffractometer, using CuKα_1 radiation (λ = 1.5406 Å) and an X'Celerator detector in Bragg–Brentano geometry. XRD patterns were recorded in the 2θ range from 10° to 90° and analysed using X'Pert Highscore Plus software. The lattice parameter (a) was extracted by fitting the reflection peaks with a Gaussian function and solving the equation for a cubic system.[26]

The oxygen non-stoichiometry was calculated from the data of thermogravimetric (TG) measurements, which were performed on a Mettler-Toledo StarE balance under dry air and N_2 flow in the range of 300–1273 K, following a heating ramp of 5 K min^{-1}. The calculations were done by taking into account that the mass loss corresponds to oxygen release (after a drying step). To obtain the final non-stoichiometry, the total O_2 mol per mol of fluorite has been added to the oxygen of the totally reduced fluorite in N_2, following the equation:

$$2 - \delta = \frac{n_{O_2}}{n_{\text{fluorite}}} + \left(2 - \frac{x}{2}\right)$$

Temperature-programmed desorption (TPD) measurements were performed in order to monitor the oxygen release with change in temperature. The sample powder (100 mg) was placed in a quartz reactor, and heated in air up to 1273 K and cooled down in the same atmosphere. Next the sample was heated at 10 K min^{-1} up to 1273 K in Ar, and the oxygen release was monitored by following the m/z = 32 and 16 amu with a mass spectrometer Omnistar (Balzers).

UV-vis spectra of the compounds were recorded on a Varian 5000 UV-Vis-NIR spectrophotometer in the range of 200–800 nm using $BaSO_4$ as a reference material and with a lamp change at 350 nm.

Rectangular probes ($4 \times 0.4 \times 0.2\ cm^3$) of the powders fired at 1073 K were uniaxially pressed at 125 MPa for 1 min and subsequently sintered for 5 h at 1573 K in air. Electrical conductivity measurements were conducted with a standard four-point DC technique on the sintered rectangular bars using silver wire and paste for electrical contact. The measurements were carried out in the temperature range from 673 to 1073 K by cooling down (1 K min^{-1}) in different O_2-containing atmospheres (Linde calibrated gas mixtures). The corresponding oxygen partial pressures were measured using a home-made YSZ oxygen sensor. The constant current was supplied by a programmable current source (Keithley 2601) and the voltage drop across the sample was measured by a multimeter (Keithley 3706). Prior to measurements, the samples were equilibrated for 2 h at the highest temperature (1073 K). Experimental data were analysed on the basis of Arrhenius behaviour $\sigma(T) = (A/T)\exp(-E_a/kT)$. The activation energy E_a was extracted from the slope of the graphs.

Sintered pellets of CT20 and CT20Co were quenched from 1073 K in air to liquid N_2 to imitate the surface conditions in PIE experiments. During the quenching experiment gaseous air was bubbled into the liquid N_2 in order to prevent sudden surface reduction of the specimen. These specimens were analyzed by X-ray photoelectron spectroscopy (XPS). Measurements were carried out on a SPECS spectrometer with a MCD-9 detector, using a non-monochromatic Al K (1486.6 eV) X-ray source. Spectra were recorded using an analyzer with a pass energy of 30 V, and an X-ray power of 100 W, under an operating pressure of 10^{-9} mbar. Spectra were analyzed using the CASA software.

 This journal is © The Royal Society of Chemistry 2013

Published on 20 June 2013. Downloaded by Universitat Politècnica de València on 29/07/2013 11:46:36.

Binding energies (BEs) were referenced to the C 1s peak at 284 eV. The energy regions of Ce 3d, Tb 3d, Tb 4d, Co 2p, O 1s and C 1s transitions were recorded for all samples.

For pulse-response isotope exchange (PIE) experiments, the powder was uniaxially pressed at 400 MPa. The disk was sintered at 1723 K for 10 h in air, and crushed into a coarse powder. The fraction passing through a 125 μm stainless steel sieve was pre-annealed at 1473 K for 10 h in air, and sieved again to remove the formed agglomerates. Prior to exchange measurements, the powders were characterized by X-ray diffraction (Philips PANalytical PW1830), BET surface area (Micromeritics Gemini ASAP 2020 M), and particle size (Malvern Mastersizer 2000) measurements. The average particle size was in the range of 0.545–0.676 μm. The surface area calculated by the BET method was found to be in the range of 0.24–0.37 (±0.01) $m^2\ g^{-1}$. The PIE measurements were performed in the temperature range of 773–1123 K at a pO_2 of 0.21 atm, using a continuous flow packed-bed micro-reactor. For the measurement, approximately 80–100 mg of sample powder was loaded between two quartz wool plugs in a quartz tubular microreactor with an inner diameter of 2 mm. The length of the packed-bed was about 10 mm. A $^{16}O_2$/Ar gas mixture was used as the carrier gas with a flow rate of 50 ml min^{-1} (NTP). The response to an $^{18}O_2/N_2$ pulse (500 μl), with the same pO_2 as the carrier gas, passing through the reactor was analyzed by online mass spectrometry (Omni Star TM GSD 301 Pfeiffer-Vacuum) at the exit of the reactor. A six-port valve with a sample loop was used for injection of the $^{18}O_2/N_2$ pulse into the $^{16}O_2$/Ar carrier gas flow stream. Oxygen isotope gas (>97 atom% $^{18}O_2$) was purchased from Cambridge Isotope Laboratory. Nitrogen used as a diluent gas was also used for internal calibration of the mass spectrometer. Prior to measurements, the powder packed-bed was pre-treated *in situ* at 1073 K for 0.5 h under flowing synthetic air in order to remove the possibly adsorbed water and CO_2, and subsequently cooled to room temperature at a rate of 5 K min^{-1}. The PIE measurements were performed, at $pO_2 = 0.21$ atm, in the temperature range of 773–1123 K. The reactor was equilibrated for 0.5 h at each temperature prior to data acquisition. The packed-bed microreactor was designed to approximate ideal plug flow behavior.[16] The isotopic exchange measurements are detailed by Yoo *et al.*[27]

Results and discussion

Structural characterization

XRD patterns of CTx and CTxCo sintered at 1723 K showed that all the powders are single phase with a cubic fluorite structure. Previous studies on the microstructure of (Co free) Tb-doped ceria showed the presence of nano-sized precipitates in the fluorite-structured matrix, which are Tb^{3+} and Ce^{3+} rich.[28] Within experimental error, diffraction peaks corresponding to any precursor or secondary phase related to Tb or Co oxides could not be detected in the present study (ESI S1†).

Fig. 1 shows the cell parameter dependence on the dopant amount for CTx and CTxCo. Also theoretical Vegard's slope for total Tb^{3+} and Tb^{4+} substitution is drawn. Vegard's law is the empirical linear relationship at constant temperature between the crystal lattice parameter and the concentrations of the dopant element. Deviations from this line may indicate the non-solubility of the dopant.[29–31] However, single-phase fluorite without impurities was observed for all samples. Thus, these deviations indicate that Tb is in a mixed 4+/3+ valence that indeed follows a linear trend with a starting 64% of Tb^{3+} for CTx and 60% for CTxCo measured at room temperature.

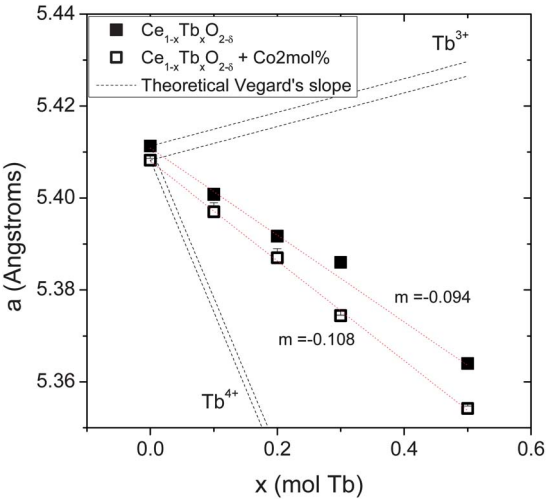

Fig. 1 Cell parameter dependence on the dopant amount for CTx and CTxCo and theoretical Vegard's slope for Tb^{3+} and Tb^{4+} total substitution.‡

As previously reported,[32] cobalt is a sintering aid enabling lowering of the densification temperature for different doped ceria. ESI S2† shows the change of the microstructure and the cobalt location, as obtained by SEM. As inferred from the XRD results displayed in Fig. 1, Co-containing compounds have a slightly smaller cell parameter than that found for Co-free samples, which is attributed to partial incorporation of Co cations into the ceria lattice; the remainder of Co resides at the grain boundary, as discussed elsewhere.[17]

The Co addition slightly increases Vegard's slope, due to the shrinkage of the cell parameter when compared to Co-free samples, which provides an indication of the higher average oxidation state of Tb cations in the Co-containing compounds, *i.e.*, smaller oxygen non-stoichiometry. Therefore, a higher reducibility of Tb^{4+} to Tb^{3+} and a different redox catalytic activity are expected for Co-containing specimens.

‡ The slopes were calculated from Vegard's law, taking the experimental Tb undoped ceria cell parameter ($x = 0$), which gave a correction factor from perfect fluorite (5.427 Å) of 0.9971 and 0.9965 for CTx and CTxCo, respectively.[29,30]

$$a(x, r_M) = 5.411 + 2.293(r_M - 1.024)x$$

$$a(x, r_M) = 5.408 + 2.292(r_M - 1.024)x$$

where $r_M(Tb^{4+}) = 0.88$ Å and $r_M(Tb^{3+}) = 1.04$ Å for the cations in eight-fold coordination according to Shannon.

Published on 20 June 2013. Downloaded by Universitat Politècnica de València on 29/07/2013 11:46:36.

Temperature-programmed desorption and oxygen non-stoichiometry

The results of TPD measurements in Ar for samples investigated in this study are shown in Fig. 2a. For CT10 oxygen desorption starts at ~750 K, reaching a maximum value at 940 K. This oxygen release suggests the reduction of the material through the concurrent cation reduction and oxygen vacancy formation. Since Ce^{4+} reduction is reported to initiate at oxygen partial pressures lower than 10^{-10} atm, and to be nearly constant at higher oxygen contents,[33–35] the changes in oxygen non-stoichiometry observed under these oxidizing conditions (>10^{-5} atm) are most likely related to reduction of Tb^{4+} rather than to reduction of Ce^{4+}. A higher dopant content is found to shift oxygen release to lower temperatures, corresponding to an increased reducibility of the material.

Co-containing samples show two distinguishable redox processes: (1) oxygen release associated with Tb^{4+} reduction, which starts at lower temperatures, *i.e.*, at *ca.* 600 K with respect to the Co-free samples and (2) a well-defined reduction process that takes place at temperatures in the range of 1000–1150 K and reaches a maximum at 1050 K, 1070 K, and 1080 K for CT10Co, CT20Co, and CT50Co, respectively. This high-temperature reduction process can be ascribed to:

(1) Reduction of Co itself ($Co^{3+} \rightarrow Co^{2+}$).[17,36] Note that the intensity of the Co-related peak changes due to the Tb background.

(2) Further reduction of bulk Tb^{4+} to Tb^{3+} as confirmed by the existence of a broadened peak at higher temperatures.

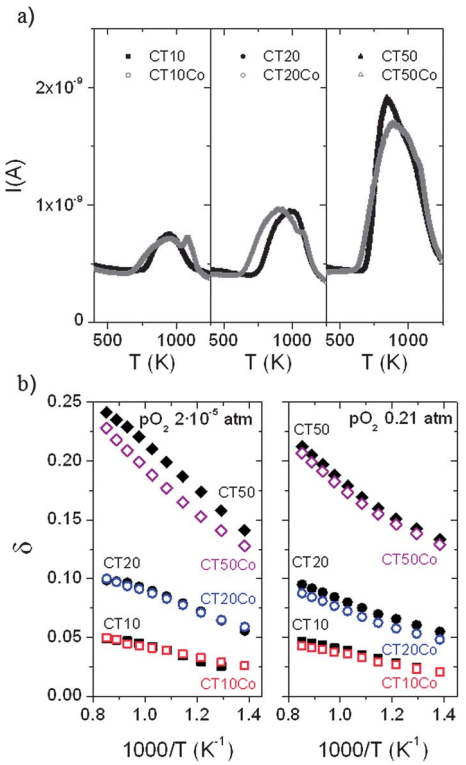

Fig. 2 (a) TPD of oxygen in Ar and (b) oxygen non-stoichiometry (δ in CTx) determined by TG in N_2 and air for CT10, CT10Co, CT20, CT20Co, CT50, CT50Co.

In summary, TPD measurements demonstrate that addition of higher amounts of Tb and Co to ceria increases the oxygen release properties. Fig. 2b shows the evolution of the oxygen non-stoichiometry parameter δ in N_2 with temperature for different samples, as determined by thermogravimetry. As expected, at high temperatures δ is not affected by the Co addition while only minor changes in δ are observed at low temperatures. On the other hand, a substantial change in δ arising from the Co addition is observed for the sample with 50% Tb (CT50Co). In fact, the lower δ observed in CT50Co with respect to CT50 seems to be associated with the higher concentration of Tb^{4+} at lower temperatures, which also emerges from the data of XRD recorded at room temperature (Fig. 1).

Conductivity and UV-vis absorption

Fig. 3a shows the dependency of the total conductivity of CTx and CTxCo on the Tb dopant concentration under air (left figure) and Ar ($pO_2 = 2 \times 10^{-5}$ atm, right figure). The total conductivity in air increases with the Tb dopant concentration, which is interpreted to reflect the enhanced concentration of oxygen vacancies at higher Tb doping levels. Under Ar the total conductivity reaches a maximum at about $x = 30$ mol% Tb. For CT50 and CT50Co, the total conductivity is found to decrease with decreasing pO_2 as seen from Fig. 3b. This observation can be attributed mainly to a p-type electronic conductor behavior. In this case, the conductivity decreases with the decrease in pO_2 since the formation of oxygen vacancies decreases the electron–hole density. The activation energy (see ESI S3†) is consistent with the electronic hopping mechanism. Besides, defect association between dopant Tb^{3+} cations and oxygen vacancies can occur, according to

$$Tb'_{Ce} + V_O^{\cdot\cdot} \leftrightarrow \left(Tb'_{Ce}V_O^{\cdot\cdot}\right) \quad (1)$$

These associated defects prevent oxygen vacancies to move and, consequently, the ionic conductivity reduces as well.[37]

Fig. 3b presents the total conductivity for different samples, at 1073 K, measured as a function of pO_2. The plot shows that (1) in general, the conductivity is enhanced by cobalt addition and (2) the conductivity-pO_2 behavior depends on the Tb content.

The total conductivity of the CT10 sample follows a $pO_2^{-1/6}$ dependency (the slope −1/6 in the graph) due to the reduction and formation of oxygen vacancies in the material when the pO_2 decreases, up to a plateau at $pO_2 \approx 10^{-3}$ atm. This behavior can also be observed in CT10Co even though the increase in conductivity is not only due to the oxygen vacancies but also due to enhanced densification of the sample. It has been reported that the use of Co as a sintering aid may result in a decrease of grain boundary resistance.[33,38] In a previous study, the maximum solubility of the Co into the ceria lattice was determined to be 1.3 mol%.[17] The remaining Co appears as a cobalt-rich phase at the grain boundary (below the detection limit of the XRD device). This cobalt-rich phase might act as a percolating network, increasing the electronic conductivity as observed for other doped ceria.[38] A beneficial effect is that the catalytic activity for the oxygen reduction reaction at the surface

 This journal is © The Royal Society of Chemistry 2013

Published on 20 June 2013. Downloaded by Universitat Politècnica de València on 29/07/2013 11:46:36.

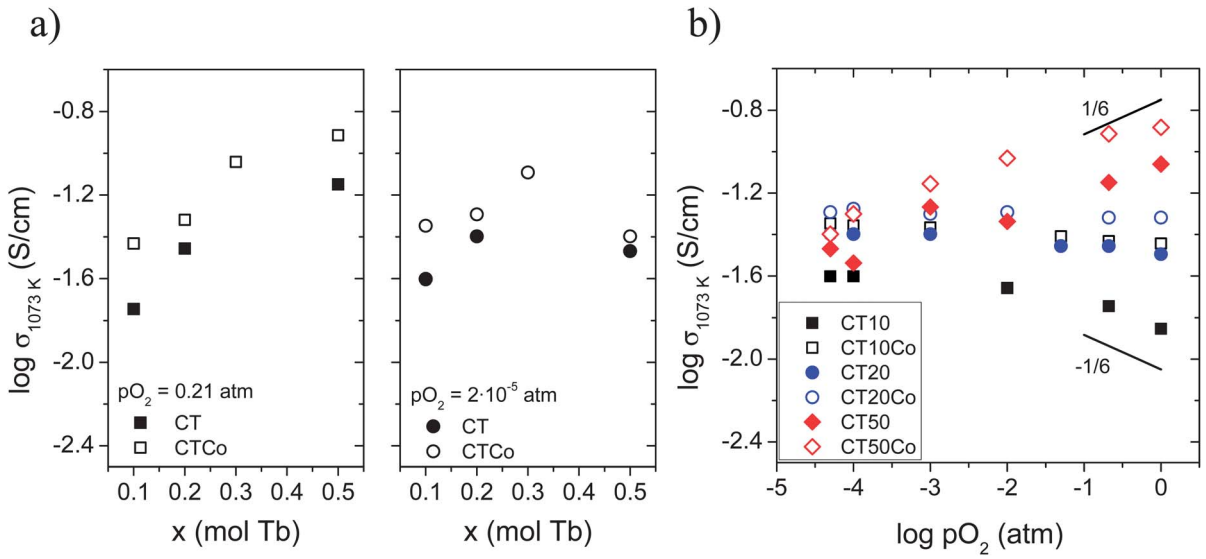

Fig. 3 Dependence of the total conductivity of CTx and CTxCo as a function of dopant concentration (x in $Ce_{1-x}Tb_xO_{2-\delta}$), at 1073 K, as measured in (a) air and Ar ($pO_2 = 2 \times 10^{-5}$ atm) and (b) as a function of pO_2.

may change due to the presence of Co, which will be discussed below.

The total conductivity found for CT20, at 1073 K, in argon is twice higher than that observed for CT10, and this increase corresponds to the increase of oxygen vacancies with the introduction of Tb into the lattice. This fact suggests that ionic conduction is the most important contribution to the total conductivity for these two compositions. The pO_2 dependency of the conductivity for CT20 is lower than $-1/6$ and reaches the ionic plateau at higher pO_2 than for CT10. It may be the consequence of the introduction of energetic levels of Tb into the ceria band gap, which permit electrons to hop from Tb^{3+} to Tb^{4+}, and the concurrent enhancement of the electronic conductivity. The small addition of Co oxide allows further increase of the p-type electronic conductivity. Particularly, this conductivity plateau is observed in the whole pO_2 range studied for CT20Co. The slight increase in conductivity observed for these samples with decreasing pO_2 is still attributed to Tb^{4+} reduction with concomitant formation of oxygen vacancies.[36]

The total conductivity of CT50 is proportional to $pO_2^{1/6}$, which is ascribed to predominant p-type conductivity. For highly Tb-doped ceria, the impurity band contributing to the electron–hole hopping and causing additional electronic transport is more evident.[41] This small polaron hopping requires the mixed valent Tb, since electrons at Tb^{3+} sites can only hop to an adjacent Tb site if it is empty, *e.g.* in the Tb^{4+} state. The maximum contribution to the electronic conductivity is, therefore, pO_2 dependent, and it will be reached when the concentration of the two valence states is equal.[37] These results confirm that electron–hole transport is the dominant conduction mechanism at high pO_2 for CT50.

UV-vis absorption experiments were carried out in order to study the influence of the dopant on the band gap. The band gap reflects the energy difference between valence and conduction bands, being related to the extent of the electronic conductivity of the material. In fact, the optical band gap energy is comparable to the thermal band gap related to the formation of electron–hole pairs. Kubelka–Munk (K–M) theory has been used to estimate the forbidden energy gap E_g of the material.[39,40] Evaluation involves plotting of the obtained $(h\nu F(R\infty)^2)$ as a function of $h\nu$. The band gap E_g can be obtained by extrapolating a tangent line drawn in the point of inflection of the curve to zero, *i.e.* the point of intersection with the $h\nu$ horizontal axis.

Fig. 4 shows the room temperature UV-vis absorption spectra of the Tb-doped series. CeO_2 and Tb_4O_7 were taken as the reference (see the inset in Fig. 4). The energy gaps for CeO_2 and Tb_4O_7 are found to be 3.3 eV and 1.94 eV, respectively. The band gap energy decreases upon Tb doping, decreasing monotonically from the pure ceria to Tb_4O_7. This fact suggests that Tb doping makes electron hopping easier and increases electronic–hole conductivity. For low Tb content materials ($x = 0.1, 0.2$) the addition of Co results in even smaller values for E_g. CT50 had the lowest E_g, which is not further lowered by the addition of Co.

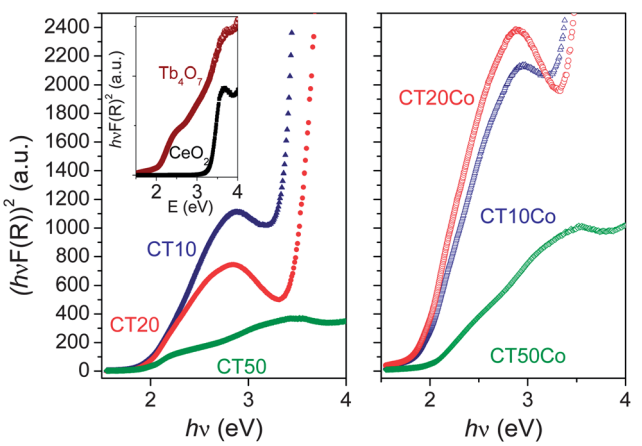

Fig. 4 UV-vis $(h\nu F(R))^2$ spectra *versus* $h\nu$ photon energy of CTx and CTxCo series.

Published on 20 June 2013. Downloaded by Universitat Politècnica de València on 29/07/2013 11:46:36.

X-ray photoelectron spectroscopy

Near-surface defect chemistry plays an important role in determining the chemical surface chemistry and gas exchange activity. Therefore, X-ray photoelectron spectroscopy (XPS) has been performed to gain insight into the position of both (1) valence bands and (2) core levels of the atoms present in the first layer of the material surface. To this end, samples of CT20 and CT20Co were quenched from 1073 K under air stream to liquid nitrogen in order to have the same material state as for the conductivity and PIE measurements.

The Ce 3d XPS spectra of CT20 and CT20Co quenched in air from 1073 K are plotted in Fig. 5. Both of them show three peaks, separated by several eV for each of the spin-orbit split 5/2; 3/2 components (more details are given in the ESI, S4†). The $3d_{3/2}$ and $3d_{5/2}$ contributions are represented as u and v, respectively. The intense u‴ component at 915.5 eV, which represents a fingerprint of the Ce^{4+} state, does not overlap with other peaks. This peak is coupled with v‴ (897.2 eV) and they both come up from an almost pure $4f^0$ electron configuration.[41] Besides, good separation between v (881.3 eV) and v″ (888.1 eV) peaks can be discerned, which is characteristic of only the Ce^{4+} state.[41,42] The whole spectrum is shifted about 1 eV to lower BE with regard to literature spectra for Ce 3d and this deviation is ascribed to charge shifting of the device. There are slight differences in the peak separation between CT20 and CT20Co, which are attributed to experimental errors rather than to a mixture of oxidation states. Ce^{3+} peaks represented as v_0 and u_0 are expected in these spectra at around 879.6 and 898.3 eV, respectively (marked by dotted vertical lines).[43] Here, it can be seen that the latter peaks do not appear, which confirms that there is a negligible amount of Ce^{3+} in the samples. Under the conditions of the experiment, no significant changes in the cerium oxidation state are found which can be associated with the presence of cobalt in the samples.

The most intense core level for terbium is Tb 3d at the high binding energy between 1230 and 1290 eV. However, it is difficult to distinguish accurately the chemical states of the Tb 3d line as the binding energies for the different oxidation states are very similar. Fig. 6 shows the Tb 3d XPS patterns of quenched samples. Two principal components are commonly distinguished related to Tb $3d_{3/2}$ and the Tb $3d_{5/2}$ binding energy peak positions. These are shifted from those published previously for pure $TbO_{1.5}$ (Tb^{3+}), where the Tb $3d_{5/2}$ and Tb $3d_{3/2}$ peaks are reported to be found at about 1239.1 and 1274 eV. Tb^{4+} related peaks appear at 1244 and 1278 eV.[44] In addition to the main peaks, terbium shows relatively intense satellites in the Tb $3d_{5/2}$ component at 1251.5 eV for the tetravalent state and 1250.6 eV for the trivalent state, and at 1264 eV for the Tb $3d_{3/2}$ component of Tb^{4+}.[45] In Fig. 6, the spectra show two peaks at 1241.6 and 1276.3 eV, and 1240.9 and 1275.7 eV for CT20Co and CT20, respectively. Also two satellites appear between the main peaks. These results suggest that Tb substituted for Ce in CeO_2 appears in more than one oxidation state, *i.e.*, 3+ and 4+.[46] The CT20Co spectrum is more shifted to higher energies, with regard to the CT20 spectrum, and this indicates a higher oxidation state, *i.e.* higher amount of Tb^{4+}. From the deconvolution of the spectra it is possible to estimate that the fractions of Tb^{3+} in the surface of CT20 and CT20Co are 60.5% and 54%, respectively. The surface oxidation state of Tb differs from the *bulk* oxidation state determined by the non-stoichiometry estimated from TG measurements in air (1073 K), *ca.* 88.5% for CT20 and 81% for CT20Co. Nevertheless, XPS results support the presence of Tb in both 3+ and 4+ oxidation states inferred from the lattice parameter extracted from the XRD of CT20 and CT20Co.

The presence of Co atoms on the grain surface is confirmed by the data from XPS. The binding energy (BE) values of the Co $2p_{3/2}$ core-level are close to 780 eV for Co^{2+} on CoOx. The main peak (red) is accompanied by a relatively intense satellite peak (blue) at 787.5 eV, characteristic of Co^{2+} species and its interaction with other metals.[47] The spin-orbital splitting upon ionization between $2p_{3/2}$ and $2p_{1/2}$ is 16 eV. XPS spectra of CT20Co in the Co 2p region are shown in Fig. 7. The low intensity of the Co 2p region is due to the very low Co content (2 mol%). The BE of the Co $2p_{3/2}$ peak is *ca.* 780 eV and the satellite peak at 787.5 eV. These binding energies correspond to

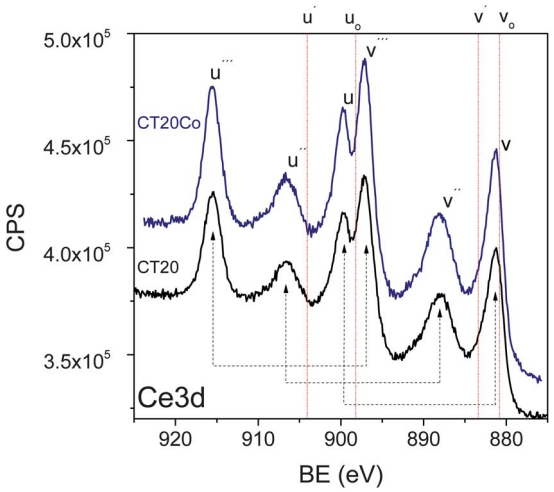

Fig. 5 Ce 3d XPS patterns of CT20 and CT20Co quenched in air from 1073 K (pass energy was 30 eV).

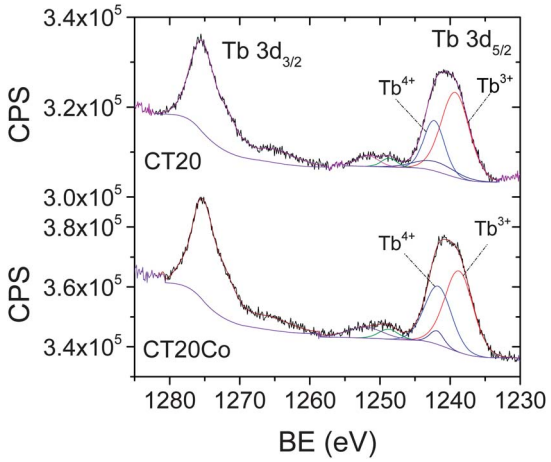

Fig. 6 X-ray photoelectron spectrum of the Tb 3d region of CT20 (a) and CT20Co (b) quenched in air from 1073 K, acquired with a pass energy of 30 eV.

 This journal is © The Royal Society of Chemistry 2013

Published on 20 June 2013. Downloaded by Universitat Politècnica de València on 29/07/2013 11:46:36.

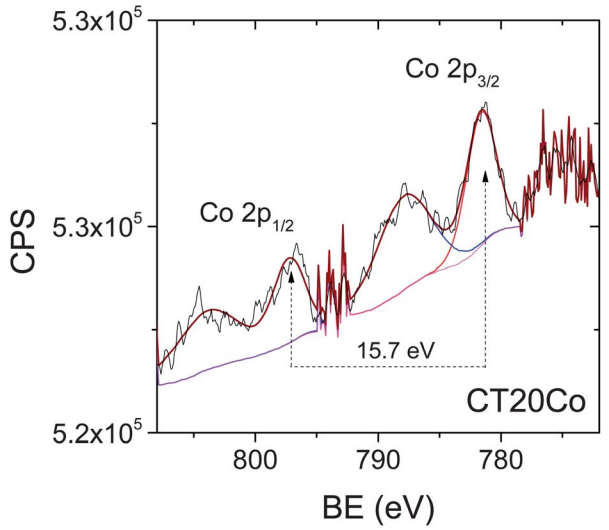

Fig. 7 X-ray photoelectron spectrum of the Co 2d region of CT20Co quenched in air from 1073 K, acquired with a pass energy of 30 eV. The Co 2d peak is shifted to higher binding energy than found in CoO (778 eV), suggesting Co lattice substitution.

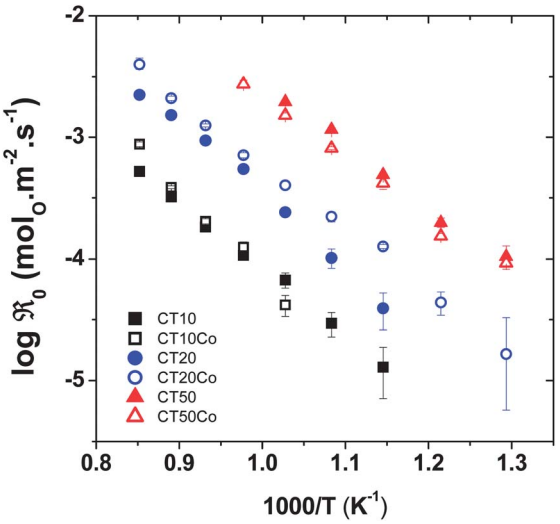

Fig. 8 Arrhenius plots of the exchange rates of CT10, CT10Co, CT20, CT20Co, CT50, and CT50Co.

cobalt oxide species highly dispersed and with a strong interaction with the structure, which may support partial incorporation of Co into the lattice of CeO_2. The BE is shifted to lower values (about 0.2 eV) compared to that of Co $2p_{3/2}$ in Co_3O_4 or CoO (780.2 eV).[48] The close proximity of binding energies for both oxides, *i.e.*, Co_3O_4 and CoO, makes it difficult to identify the Co state at the surface of this material.

Pulse isotopic exchange

The rate of oxygen surface exchange on Tb-doped ceria may be influenced by the surface concentration of oxygen vacancies and by the *supply* of electrons, which are necessary for charge transfer.[49] Fig. 8 displays Arrhenius plots of the overall exchange rate ($\Re_0$) for all materials investigated in this study as evaluated from the data of pulse isotopic exchange (PIE) measurements. $\Re_0$ is found to increase profoundly with increasing Tb concentration. The data listed in Table 1 support a relationship between the surface exchange rate, at 973 K, and the corresponding concentration of oxygen vacancies in the Tb-doped ceria samples (see also ESI S6†).

Note from Fig. 8 that Co addition to either CT10 or CT50 does not significantly improve $\Re_0$. However, Co is found to improve the surface exchange rate when added to CT20. These observations support the conclusion that the rate of exchange in these materials is determined by (i) the concentration of oxygen vacancies, which is related to the ionic conductivity, (ii) the (p-type) electronic conductivity, and (iii) the balance between these two parameters.

PIE experiments also provide information about the surface exchange mechanism.[23] The distribution of oxygen isotopomers ($^{18}O_2$, $^{16}O^{18}O$, $^{16}O_2$) in the effluent pulse can be modeled by adopting a two-step exchange mechanism, in which isotopic scrambling is determined by the rate of dissociative adsorption of O_2 molecules at the surface and that of successive

Table 1 Oxygen non-stoichiometry and surface exchange rate, at 973 K, and apparent activation energies for the surface exchange rate for different compounds (for more details see ESI Fig S5†)

Compound	δ (973 K)	$\Re_0$ (mol O per m^2 per s) (973 K)	E_a (kJ mol^{-1}) [temperature range]
CT10	0.042	6.71×10^{-5}	105 [873–1173 K]
CT10Co	0.036	4.18×10^{-5}	136 [973–1173 K]
CT20	0.08	2.42×10^{-4}	118 [873–1173 K]
CT20Co	0.073	4.02×10^{-4}	101 [773–1173 K]
CT50	0.179	1.96×10^{-3}	96 [773–973 K]
CT50Co	0.174	1.52×10^{-3}	97 [773–1023 K]

incorporation of adsorbed O adatoms into the oxide lattice. The overall rate of surface exchange on both undoped and Co-doped CTx samples appears to be controlled by the dissociative adsorption reaction, as was found for, *e.g.*, 25 mol% erbia-stabilized bismuth oxide (BE25)[27] and $Ba_{1-x}Sr_xCo_{0.8}Fe_{0.2}O_{3-\delta}$ (BSCF).[23] For all compositions studied, the rate of oxygen incorporation was found between one or two orders of magnitude higher (ESI S7†). The observations made in this study can be reconciled by assuming that O_2 dissociative adsorption and, hence, overall oxygen exchange are rate determined by electron transfer to intermediate superoxide ions (O_2^-) at the surface

$$O_2^- + e^- \rightarrow 2O^- \quad (2)$$

with the notion that surface oxygen vacancies are assumed to be the sites at which adsorption of O_2 molecules takes place.

Conclusions

Tb-doped ceria materials were prepared by the co-precipitation method. Cobalt oxide (2 mol%) was added to improve sinterability and electronic conductivity. Results of the

Published on 20 June 2013. Downloaded by Universitat Politècnica de València on 29/07/2013 11:46:36.

characterization by XRD and total conductivity suggest that only part of the cobalt is incorporated into the ceria lattice. The conductivity results indicate that the extent of mixed ionic–electronic conductivity is a function of temperature and can be tuned by modifying the Tb- (and Co-doping) concentration. Low Tb content materials ($x = 0.1$) show predominantly ionic conductivity. CT50 and CT50Co materials show p-type electronic conductivity combined with a higher ionic conductivity, which is related to the higher oxygen non-stoichiometry. The enhanced electronic conductivity is due to the introduction of an impurity band into the band gap of ceria upon doping with Tb.

The oxygen exchange rate of CTx and CTxCo materials was measured using PIE. The highest surface exchange rates were obtained for CT50 and CT50Co samples. On the whole, the results indicate that the exchange rate exhibited by CTx is limited by the dissociative adsorption of molecular oxygen at the oxide surface, and its magnitude is bound by the relative magnitudes of the ionic and electronic conductivities in the materials.

Acknowledgements

Funding from the Spanish Government (BES-2009-015835, ENE2011-24761 and SEV-2012-0267 grants) and Helmholtz Association (MEM-BRAIN Portfolio) is kindly acknowledged.

Notes and references

1 M. B. Toftegaard, J. Brix, P. A. Jensen, P. Glarborg and A. D. Jensen, *Prog. Energy Combust. Sci.*, 2010, **36**, 581.
2 M. P. Lobera, M. Balaguer, J. García-Fayos and J. M. Serra, *ChemCatChem*, 2012, **4**, 2102.
3 J. Sunarso, S. Baumann, J. M. Serra, W. A. Meulenberg, S. Liu, Y. S. Lin and J. C. Diniz da Costa, *J. Membr. Sci.*, 2008, **320**, 13.
4 M. L. Fontaine, Y. Larring, T. Norby, T. Grande and R. Bredesen, *Ann. Chim. Sci. Mat.*, 2007, **32**, 197.
5 J. M. Serra, V. B. Vert, O. Büchler, W. A. Meulenberg and H. P. Buchkremer, *Chem. Mater.*, 2008, **20**, 3867.
6 A. Leo, S. Smart, S. Liu and J. C. Diniz da Costa, *J. Membr. Sci.*, 2011, **368**, 64.
7 S. Liu, X. Tan Shao and J. C. Diniz da Costa, *AIChE J.*, 2006, **52**, 3452.
8 S. Baumann, J. M. Serra, P. Lobera, S. Escolástico, F. Schulze-Küppers and W. A. Meulenberg, *J. Membr. Sci.*, 2011, **377**, 198.
9 X. Tan and K. Li, *AIChE J.*, 2007, **53**, 838.
10 M. Arnold, H. Wang and A. Feldhoff, *J. Membr. Sci.*, 2007, **293**, 44.
11 Z. P. Shao, W. S. Yang, Y. Cong, H. Dong, J. H. Tong and G. Xiong, *J. Membr. Sci.*, 2000, **172**, 177.
12 A. Leo, S. Liu and J. C. Diniz da Costa, *Int. J. Greenhouse Gas Control*, 2009, **3**, 357.
13 J. H. Park, J. P. Kim and S. H. Son, *Energy Procedia*, 2008, **1**, 369.
14 M. Balaguer, C. Solís and J. M. Serra, *J. Phys. Chem. C*, 2012, **116**, 7975.
15 D. P. Fagg, A. L. Shaula, V. V. Kharton and J. R. Frade, *J. Membr. Sci.*, 2007, **299**, 1.
16 C. Chatzichristodoulou, P. V. Hendriksen, A. Hagen and J. C. Grivel, *ECS Trans.*, 2008, **13**, 347.
17 M. Balaguer, C. Solís and J. M. Serra, *Chem. Mater.*, 2011, **23**, 233.
18 M. P. Lobera, J. M. Serra, S. P. Foghmoes, M. Søgaard and A. Kaiser, *J. Membr. Sci.*, 2011, **385**, 154.
19 H. Luo, K. Efimov, H. Jiang, A. Feldhoff, H. Wang and J. Caro, *Angew. Chem.*, 2011, **50**, 759.
20 F. Mauvy, J. M. Bassat, E. Boehm, P. Dordor, J. C. Grenier and J. P. Loup, *J. Eur. Ceram. Soc.*, 2004, **24**, 1265.
21 K. Yashiro, S. Onuma, A. Kaimai, Y. Nigara, T. Kawada, J. Mizusaki, K. Kawamura, T. Horita and H. Yokokawa, *Solid State Ionics*, 2002, **152**, 469.
22 P. Haworth, S. Smart, J. M. Serra and J. C. Diniz da Costa, *Phys. Chem. Chem. Phys.*, 2012, **14**, 9104.
23 H. J. M. Bouwmeester, C. Song, J. Zhu, J. Yi, M. van Sint Annaland and B. A. Boukamp, *Phys. Chem. Chem. Phys.*, 2009, **11**, 9640.
24 E. N. Armstrong, K. L. Duncan, D. J. Oh, J. F. Weaver and E. D. Wachsman, *J. Electrochem. Soc.*, 2011, **158**, B492.
25 H. J. M. Bouwmeester, M. W. den Otter and B. A. Boukamp, *J. Solid State Electrochem.*, 2004, **8**, 599–605.
26 A. Kumar, S. Babu, A. S. Karakoti, A. Schulte and S. Seal, *Langmuir*, 2009, **25**, 10998.
27 C. Y. Yoo, B. A. Boukamp and H. J. M. Bouwmeester, *J. Solid State Electrochem.*, 2011, 231.
28 F. Ye, T. Mori, D. R. Ou, J. Zou and J. Drennan, *Mater. Res. Bull.*, 2007, **42**, 943.
29 D. J. Kim, *J. Am. Ceram. Soc.*, 1989, **72**, 1451.
30 S. J. Hong and A. V. Virkar, *J. Am. Ceram. Soc.*, 1995, **78**, 433.
31 D. P. Fagg, J. R. Frade, M. Mogensen and J. T. S. Irvine, *J. Solid State Chem.*, 2007, **180**, 2371.
32 J. D. Nicholas and L. C. De Jonghe, *Solid State Ionics*, 2007, **178**, 1187.
33 D. P. Fagg, S. García-Martín, V. V. Kharton and J. R. Frade, *Chem. Mater.*, 2009, **21**, 381.
34 D. P. Fagg, I. P. Marozau, A. L. Shaula, V. V. Kharton and J. R. Frade, *J. Solid State Chem.*, 2006, **179**, 3347.
35 K. L. Duncan, Y. Wang, S. R. Bishop, F. Ebrahimi and E. D. Wachsman, *J. Appl. Phys.*, 2007, **101**, 044906.
36 C.-W. Tang, C.-B. Wang and S.-H. Chien, *Thermochim. Acta*, 2008, **473**, 68.
37 H. L. Tuller, S. R. Bishop, D. Chen, Y. Kuru, J.-J. Kim and T. S. Stefanik, *Solid State Ionics*, 2012, **225**, 194.
38 K. Schmale, M. Grünebaum, M. Janssen, S. Baumann, F. Schulze-Küppers and H. D. Wiemhöfer, *Phys. Status Solidi B*, 2011, **248**, 314.
39 R. López and R. Gómez, *J. Sol-Gel Sci. Technol.*, 2012, **61**, 1.
40 A. B. Murphy, *Sol. Energy Mater. Sol. Cells*, 2007, **91**, 1326.
41 E. Paparazzo, *Mater. Res. Bull.*, 2011, **46**, 323.
42 B. M. Reddy, G. Thrimurthulu and L. Katta, *Chin. J. Catal.*, 2011, **32**, 800.
43 F. Larachi, J. Pierre, A. Adnot and A. Bernis, *Appl. Surf. Sci.*, 2002, **195**, 236.

 This journal is © The Royal Society of Chemistry 2013

44 I. M. Nagpure, S. S. Pitale, E. Coetsee, O. M. Ntwaeaborwa, J. J. Terblans and H. C. Swart, *Appl. Surf. Sci.*, 2011, **257**, 10147.
45 G. Blanco, J. M. Pintado, S. Bernal, M. A. Cauqui, M. P. Corchado, A. Galtayries, J. Ghijsen, R. Sporken, T. Eickhoff and W. Drube, *Surf. Interface Anal.*, 2002, **34**, 120.
46 D. D. Sarma and C. N. R. Rao, *J. Electron Spectrosc. Relat. Phenom.*, 1980, **20**, 25.
47 Z. Zsoldos and L. Cuczi, *J. Phys. Chem.*, 1992, **96**, 9393.
48 S. G. Aspromonte, A. Sastre, A. V. Boix, M. J. Cocero and E. Alonso, *Microporous Mesoporous Mater.*, 2012, **148**, 53.
49 J. Lane and J. Kilner, *Solid State Ionics*, 2000, **136**, 927.

Published on 20 June 2013. Downloaded by Universitat Politècnica de València on 29/07/2013 11:46:36.